https://dx.doi.org/10.1016/j.trgeo.2020.100336

This is the Pre-Published Version.

Numerical analysis for the role of soil properties to the load transfer in clay foundation due to the traffic load of the metro tunnel

Jie YANG[1], Zhen-Yu YIN[1,*] Xian-Feng LIU[2] and Fu-Ping Gao[3,4]

Affiliations:

[1] Department of Civil and Environmental Engineering, The Hong Kong Polytechnic University, Hung Hom, Kowloon, Hong Kong, China

[2] Key Laboratory of High-speed Railway Engineering of Ministry of Education, School of Civil Engineering, Southwest Jiaotong University, Chengdu 610031, China

[3] Key Laboratory for Mechanics in Fluid Solid Coupling Systems, Institute of Mechanics, Chinese Academy of Sciences, Beijing 100190,

[4] China School of Engineering Science, University of Chinese Academy of Sciences, Beijing 100049, China

[*] Corresponding authors: Dr. Zhen-Yu YIN, Tel: +852 3400 8470; Fax: +852 2334 6389; Emails: zhenyu.yin@polyu.edu.hk; zhenyu.yin@gmail.com

Abstract: Soil properties play important role to the metro tunnel settlement induced by traffic load of metro operation. Numerical studies on this topic are still rare due to the lack of accurate dynamic constitutive models of clay. In this study, a new critical state based bounding surface plasticity model for natural structured clays is first developed. It is able to consider the initial and induced anisotropy of natural clay and the structure disturbance to the initial size of yield surface and to the initial adhesive stress by cyclic loading at low-stress levels. The applicability of the present model is evaluated through comparisons between the predicted and the measured results of numerous stress-path tests on Shanghai clay and Vallericca stiff clay. The model is then implemented as a user-defined model in a finite difference code. A typical tunnel in clay is simulated using the implemented model coupled with Biot's consolidation, for which the stress distribution pattern in subsoils around tunnels due to train movement is investigated. The role of the dynamic constitutive model has been highlighted by comparing the simulation results of a static constitutive model and a dynamic constitutive model. The influences of the soil properties such as the anisotropy, structure ratio, and adhesive mean stress have been found significant to the load tranfer.

Keywords: Clay; anisotropy; bounding surface; traffic load; finite difference method

© 2020. This manuscript version is made available under the CC-BY-NC-ND 4.0 license http://creativecommons.org/licenses/by-nc-nd/4.0/

1. Introduction

In recent years, metro systems are being constructed in metropolitan areas all over the world. During long-term operation, the tunnel structures have suffered significant settlement and substantial differential settlement [1, 2]. For example, the maximum settlement of Shanghai metro line No. 1, which was opened in 1995, reached about 295 mm until 2010.

Many factors may have contributed to tunnel settlement, such as post-construction settlement due to tunnelling disturbance, cyclic loading of trains, groundwater infiltration, ground loss and disturbance from nearby constructions [1, 3-5]. Although the dynamic settlement is trivial for each train vibration, the accumulation of permanent deformation and excess pore pressure does occur in saturated soft clay under a long-term cyclic load [6].

Previous experimental studies have shown that the cyclic loading will lead to permanent plastic strain of clay, which accumulates at a decreasing rate as the number of cycles increases, and may even lead to failure due to the development of excess pore pressure and strain [7-11]. The factors influencing cumulative plastic strain include soil stress state, number of repeated load applications, soil type and soil physical state [12, 13]. In most cases, the traffic loading does not cause the failure of subsoil, but the cumulative plastic strain can be very significant. For example, the Saga Airport Road has a sublayer of 20 m thick compressible and highly sensitive Ariake clay, and the traffic-load-induced settlement reached 0.2 m after the road had been opened to traffic for 5 years [12]. From this perspective, the train load-induced settlement of subsoil may be one of the reasons accounting for tunnel settlement built in saturated clay.

In terms of the quantitative calculations on the train-load-induced response of tunnel and surrounding soils, numerous researches have been published using different methods, including analytical approaches [14-17], numerical simulation methods [18, 19] and empirical models [12, 20, 21]. The analytical approach can predict the dynamic response of tunnel in specific cases; however, it is usually viable for relatively simple cases, and the plastic deformation of the soil cannot be considered. For the soft clay ground, the surrounding soft clay can be easily disturbed by the frequent train vibration in the metro tunnel, which induces long-term settlement and accumulation of excess pore pressure [1, 6]. The elastoplastic behaviour of saturated soft clay should not be neglected, especially in analysing the long-term effect of train vibration. However, due to the lack of accurate dynamic constitutive models for soft clay and high computational cost, most researchers turn to empirical methods. In this case, if the load transfer in clay foundation due to traffic load of the metro tunnel is accurate enough, the simple

63 empirical or analytical models describing the permanent strain or/and pore water pressure with
64 the number of cycles can be directly applied. Thus, the estimation of load transfer in clay
65 foundation due to traffic load of the metro tunnel considering different features of clay becomes
66 crucial.

67 Therefore, this study aims to investigate the role of soil properties to the load transfer in the
68 clay foundation due to the traffic load of the metro tunnel. The rest of this paper is organized
69 as follows. First, a new critical state based bounding surface Anisotropic Structured Clay
70 Model (ASCM) is developed. It is able to consider the initial and induced anisotropy of natural
71 clay and the structure disturbance to the initial size of yield surface and to the initial adhesive
72 stress by cyclic loading at low-stress levels. The model is then validated by simulating
73 odeometer tests and triaxial tests with various stress paths on Shanghai clay and Vallericca stiff
74 clay. Then, the ASCM model is implemented as a user-defined model into a finite difference
75 code. The final part focuses on the 2D numerical calculations to investigate the load transfer in
76 the clay foundation due to the metro operation. The role of the dynamic constitutive models
77 has been highlighted by comparing the results of a static constitutive model (MCC model) and
78 a dynamic constitutive model (ASCM model). The influences of the soil's anisotropy, structure
79 ratio, and adhesive mean stress have been discussed.

80 ## 2. Constitutive model

81 The proposed model, named Anisotropic Structured Clay Model (ASCM), is based on the
82 critical state modelling framework [22] and the bounding surface plasticity concept [23].
83 According to the elastoplasticity theory, the total strain rate is additively composed of the
84 elastic strain rates and the plastic strain rates, namely,

85 $$\dot{\varepsilon}_{ij} = \dot{\varepsilon}_{ij}^{e} + \dot{\varepsilon}_{ij}^{p} \quad \text{.....(2)}$$

86 where $\dot{\varepsilon}_{ij}$ denotes the (i, j) component of the total strain rate tensor, and superscripts e and
87 p stand for the elastic and plastic components, respectively.

88 ### 2.1. Elastic behaviour

89 The elastic behaviour is assumed to be isotropic, as follows:

90 $$\dot{\varepsilon}_{ij}^{e} = \frac{1+\upsilon}{E}\sigma'_{ij} - \frac{\upsilon}{E}\sigma'_{kk}\delta_{ij} \quad \text{.....(3)}$$

91 where υ and E are Poisson's ratio and Young's modulus; σ'_{ij} is the effective stress tensor;

δ_{ij} is Kronecker's delta. The Young's modulus E can also be replaced by the elastic bulk modulus K by $E = 3K(1-2\upsilon)$. For clay, the elastic bulk modulus K can be determined by the relation [22] $K = p'(1+e_0)/\kappa$, with the mean effective stress $p' = \sigma'_{kk}/3$, the slope of the swelling line κ and the initial void ratio e_0. Assuming a common value of $\upsilon = 0.25$ for clay, only the parameter κ is needed for the elastic behaviours.

2.2. Bounding surface

The essential elements of the model in the triaxial space are schematically presented in Figure 1. Extended from the yield surface proposed first by Roscoe and Burland [22] and later-on by Dafalias [23], the bounding surface accounting for soil structure can be expressed as follows:

$$\overline{F} = \frac{3}{2}\frac{\left[\overline{s}_{ij} - (\overline{p}+p_b)\alpha_{ij}\right]:\left[\overline{s}_{ij} - (\overline{p}+p_b)\alpha_{ij}\right]}{\left(M(\theta)^2 - \frac{3}{2}\alpha_{ij}:\alpha_{ij}\right)} + (\overline{p}+p_b)\left[\overline{p} - (1+\chi)p_{ci}\right] = 0 \quad \text{.....(4)}$$

where $\overline{p}$ and $\overline{s}_{ij}$ are the mean effective and deviatoric stress tensor, respectively, and the bar indicates that these variables are related to the bounding surface; p_{ci}, α_{ij}, χ and p_b are related to hardening varables: p_{ci} is the size of intrinsic yield surface corresponding to the reconstituted sample of the clay, α_{ij} is the deviatoric fabric tensor (see Wheeler et al. [24]), $\chi = p_c/p_{ci} - 1$ is the structure ratio relating to the sizes of initial yield surface (structure surface) and the intrinsic yield surface where p_c represents the size of structure surface, p_b is the adhesive mean stress.

The Eq. (4) can be simplified in $p'-q$ plane as:

$$\overline{F} = \frac{\left[\overline{q} - (\overline{p}+p_b)\alpha\right]^2}{M(\theta)^2 - \alpha} + (\overline{p}+p_b)\left[\overline{p} - (1+\chi)p_{ci}\right] = 0 \quad \text{.....(5)}$$

M is the slope of the critical state line in triaxial space, which is defined by the Lode angle θ as follows [25]:

$$M(\theta) = M_c\left[\frac{2m^4}{(1+m^4) - (1-m^4)\sin 3\theta}\right]^{1/4} \quad \text{.....(6)}$$

where m is a material parameter defined as $m = M_e/M_c$ in which M_c and M_e are the critical

state stress ratios for triaxial compression and triaxial extension in $p-q$ stress space. According to Mohr-Coulomb yield criterion, $m=\left(3-\sin\phi_c\right)/\left(3+\sin\phi_c\right)$ (ϕ_c is the friction angle with $\phi_c=\sin^{-1}\left[3M_c/\left(6+M_c\right)\right]$), $-\pi/2\le\theta=\sin^{-1}\left(-3\sqrt{3}\bar{J}_3/2\bar{J}_2^{3/2}\right)\le\pi/2$ with $\bar{J}_2=\bar{s}_{ij}:\bar{s}_{ij}/2$, $\bar{J}_3=\bar{s}_{ij}\bar{s}_{jk}\bar{s}_{ki}/3$ and $\bar{s}_{ij}=s_{ij}-\left(p'+p_b\right)\alpha_{ij}$. This is similar to Yao et al. (2008, 2009) [26, 27].

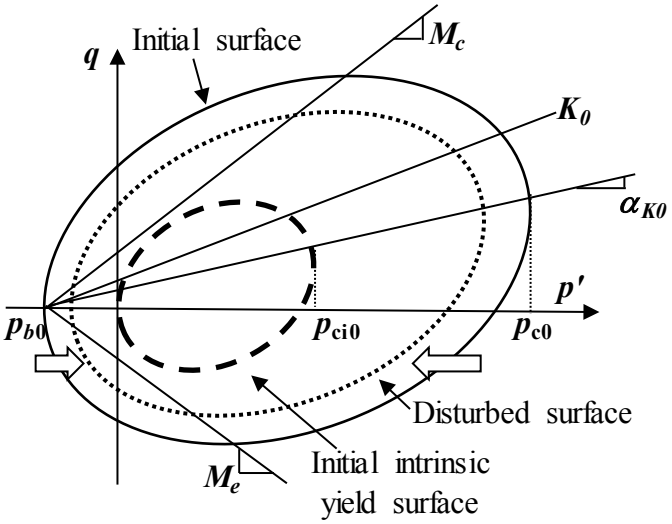

Figure 1 Schematic illustration of the loading and bounding surfaces of the model in triaxial stress space

2.3. Hardening rules

Four hardening parameters were introduced in the proposed model with four hardening rules. The isotropic (p_{ci}), rotational/anisotropic (α_{ij}) hardening rules, destructuration law (χ) and adhesive mean stress hardening law (p_b) are used to control the size, the rotation, the process of destructuration and the adhesive stress of the yield surface.

2.3.1. Isotropic hardening

In line with the Cam-clay model, a volumetric hardening rule is adopted. The intrinsic yield surface corresponding to reconstituted or fully disturbed clay expands with the plastic volumetric strain. The internal variable p_{ci} is used to reflect the effect of preconsolidation, which is independent of the bonding of soils and controls the size of the yield surface. p_{ci} is controlled only by the plastic volumetric strain rate $\dot{\varepsilon}_v^p$, given by

$$\dot{p}_{ci}=p_{ci}\frac{1+e_0}{\lambda-\kappa}\dot{\varepsilon}_v^p \quad \text{.....(7)}$$

Where λ and κ are the slope of the normal compression line and the slope of the swelling line in the $e-\ln p'$ space.

2.3.2. Rotational/anisotropic hardening

The rotational rate of the bounding surface is controlled by the evolution of the anisotropic tensor α_{ij}. We adopt a similar form to the anisotropic/rotational law proposed by Wheeler et al. [24] and the adhesive mean stress (p_b) is considered. The proposed form of modified hardening law is expressed as follow:

$$\dot{\alpha}_{ij} = \omega\left[\left(\frac{3s_{ij}}{4p'+4p_b}-\alpha_{ij}\right)\left\langle\dot{\varepsilon}_v^p\right\rangle+\omega_d\left(\frac{s_{ij}}{3p'+3p_b}-\alpha_{ij}\right)\dot{\varepsilon}_d^p\right] \quad \text{.....(8)}$$

where the parameter ω_d controls the relative effectiveness of plastic shear strains $\dot{\varepsilon}_d^p$ and plastic volumetric strains $\dot{\varepsilon}_v^p$ in determining the overall current target value for α_{ij}; and the parameter ω controls the absolute rate at which α_{ij} approaches its current target value; $\langle\ \rangle$ are the Macaulay brackets which means $\left\langle\dot{\varepsilon}_v^p\right\rangle = 0$ for $\dot{\varepsilon}_v^p \le 0$ and $\left\langle\dot{\varepsilon}_v^p\right\rangle = \dot{\varepsilon}_v^p$ for $\dot{\varepsilon}_v^p > 0$.

According to Yin et al [28-31], the anisotropic hardening parameters can be determined as follow:

$$\omega = \frac{1+e_0}{\lambda-\kappa}\lg\left(\frac{10M_c{}^2-2\alpha_{K_0}\omega_d}{M_c{}^2-2\alpha_{K_0}\omega_d}\right) \quad \text{.....(9)}$$

$$\omega_d = 3\frac{M_c{}^2-\eta_{K_0}^2-3(1-a)\eta_{K_0}}{2(\eta_{K_0}^2+3(1-b)\eta_{K_0}-M_c{}^2)} \quad \text{.....(10)}$$

with $\alpha_{K_0} = \eta_{K_0} - \left(M_c{}^2-\eta_{K_0}^2\right)/3$, $\eta_{K_0} = 3M_c/\left(6-M_c\right)$. Experimental evidence from Otaniemi clay from Finland [32] suggests $a = 3/4, b = 1/3$. Therefore, no input parameter is needed for anisotropic hardening.

2.3.3. Destructuration law

The structure surface, which can be thought of as a bounding surface, controls the process of destructuration. The structure surface for intact clay will be reduced due to the structure disturbance of soils during plastic straining. The scalar variable χ represents the progressive degradation of soils, which controls the ratio between the sizes of the structure surface and reference surface:

$$\chi = \frac{p_c}{p_{ci}} - 1 \quad (11)$$

$$\dot{\chi} = -\chi\left(\xi_c \sqrt{\delta\varepsilon_{ij}^p \delta\varepsilon_{ij}^p}\right) \quad (12)$$

where p_c is the structural yielding stress; ξ_c is a parameter which describes the rate of destructuration with plastic strain.

2.3.4. Adhesive mean stress hardening law

The adhesive mean stress is formed due to the cementation between clay particles. Similar to the yield surface, this adhesive mean stress, p_b, will be reduced due to the structure disturbance of soils during plastic straining:

$$\dot{p}_b = -p_b\left(\xi_b \dot{\varepsilon}_d^p\right) \quad (13)$$

Where ξ_b is a parameter which describes the degradation rate of p_b with the plastic shear strains. According to the experimental results on the structural clay and the stiff clay [33], the influence of the volumetric plastic strain on the evolution of adhesive stress can be neglected.

2.4. Mapping rule

In the proposed model, the projection centre is fixed at the origin of $p'-q$ stress space. And following the linear radial mapping rule (Dafalias and Herrmann [34]), for any actual stress point σ_{ij}, there is a unique image stress point $\bar{\sigma}_{ij}$ on the bounding surface corresponding to the current stress point. The following relationships are used in relating current stress states to those at the bounding surface (shown in Figure 2):

$$\bar{\sigma}_{ij} = \beta\sigma_{ij} \quad (14)$$

where β is the mapping coefficient.

Associated flow rule is adopted for this bounding surface model. Thus, the bounding surface function also serves as the plastic potential function. The plastic strain rate is determined as

$$\dot{\varepsilon}_{ij}^p = d\lambda \frac{\partial \bar{F}}{\partial \bar{\sigma}_{ij}} \quad (15)$$

where $d\lambda$ is the plastic loading index, is defined as follows

183 $$d\lambda = \frac{1}{K_p}\frac{\partial \bar{F}}{\partial \bar{\sigma}_{ij}}\delta\sigma_{ij} = \frac{1}{\bar{K}_p}\frac{\partial \bar{F}}{\partial \bar{\sigma}_{ij}}\delta\bar{\sigma}_{ij} \quad \text{.....(16)}$$

184 According to Dafalias [23], the bounding plastic modulus can be derived as:

185 $$K_p = \bar{K}_p + k_p \frac{1+e_0}{\lambda-\kappa}\left(\beta p'\right)^3\left(1-\frac{1}{\beta}\right) \quad \text{.....(17)}$$

186 where k_p is a constant for the bounding plastic modulus.

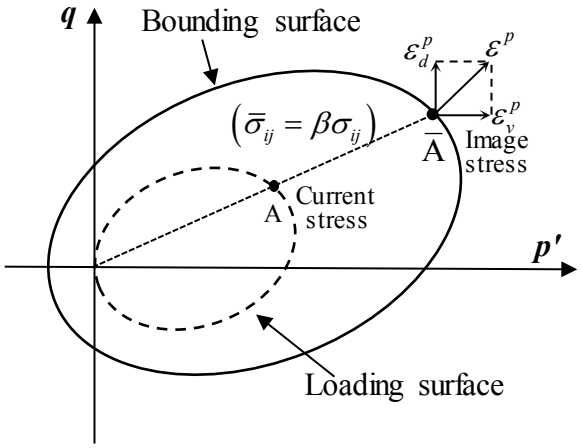

187

188 **Figure 2 Mapping rule in bounding surface model**

189 **2.5. Model parameters**

190 The proposed model requires 8 material parameters as well as the initial state parameters (e_0,
191 POP or OCR, χ_0, p_{b0}). e_0 is the initial void ratio, POP is the pre-over-consolidation pressure,
192 OCR is the over consolidation ratio, χ_0 and p_{b0} represent respectively the initial structure
193 ratio and the initial adhesive mean stress of clay. Based on their physical meanings, the
194 parameters required by this model can be divided into four groups, which are related
195 respectively to (1) critical state soil mechanics ($\lambda, \kappa, M_c, M_e, \upsilon$), (2) loss of structure (ξ_c, ξ_b),
196 and (3) plastic modulus (k_p). The procedure for determining soil parameter values and initial
197 values of the state variables for the proposed model is relatively straightforward.

198 (1) λ and κ are determined from isotropic consolidation tests. They may also be obtained
199 from the compression index C_c and swelling index C_s of one-dimensional consolidation tests,
200 where $\lambda = C_c/2.303$ and $\kappa = C_s/2.303$. M_c and M_e are determined from the slope of the
201 critical state line or indirectly from the angle of internal friction ϕ_c. Poisson's ratio υ may be
202 specified as a constant.

(2) The structure parameters (ξ_c, ξ_b) can be determined by comparing triaxial compression and one-dimensional compression tests.

(3) The parameters for plastic modulus (k_p) can be obtained by best fitting the experimental results triaxial compression tests on over-consolidated clay.

However, it should be noted that the values of parameters can also be identified either by optimisation methods [35-38] or by Bayesian based methods [39, 40]. Application of these methods can efficiently increase the accuracy in the identification of model parameters while minimising the experimental costs and efforts, i.e., the number of tests and the "trial-error" efforts.

2.6. Model validation

The experimental verification is presented herein with reference to oedometer tests and undrained triaxial tests results under monotonic loading on Shanghai clays and Vallericca stiff clay.

Oedometer test and triaxial loading tests on isotropically and anisotropically (K_0 = 0.6) compressed samples of Shanghai soft clay performed by Huang et al. [41] are simulated with the proposed model and MCC model. The calibration of material parameters was based on the results of oedometer test and isotropically consolidated specimens, so that the behaviors of anisotropically consolidated specimens were predicted. The calibrated parameters are shown in Table 1.

Figure 3 shows the comparison between the results of ASCM model, MCC model and the experimental data for odeometer test on Shanghai clay. The solid and dashed lines show the predicted results by the proposed model and MCC model, respectively. The points are the experimental results. Figure 4 presents the undrained compression behavior of Shanghai soft clay with two different isotropic consolidation pressures of 50 and 100 kPa. Figure 5 shows the comparison between the results of two models and the experimental data for two undrained compression tests on anisotropically consolidated specimens.

In the simulation of oedometer test, the proposed model can well reproduce the difference in compression characteristics before and after the damage of soil structure. Regarding the simulation of undrained triaxial tests, the general trend is well captured by the proposed model in terms of stress path and deviatoric stress versus strain response. The predicted effective stress

paths converge towards ultimate remoulded undrained strengths on the critical state line. The characters of high stiffness and strain softening for structured clay are well reflected by the proposed model. However, the results predicted by the MCC model were less satisfactory in tests on both the isotropic samples and the anisotropic samples, because the behaviors of anisotropy and structure are not estimated effectively. Under the relatively higher consolidation stress (p_0 = 100 kPa) which is on the verge of yield stress, however, the MCC model performs slightly better than under the lower consolidation stress (p_0 = 50 kPa) because of the damage of structure. At the same time, the prediction for isotropic tests is somewhat better than anisotropic tests.

Table 1 Model parameters for Shanghai clay and Vallericca clay

Model parameter	Shanghai clay	Vallericca stiff clay
ν	0.25	0.25
κ_i	0.036	0.022
λ_i	0.17	0.148
M_c	1.04	0.9
p_{c0}	68.2	1694
χ_0	4.8	1.55
ξ_c	11	20
p_{b0}	18.5	590
ξ_b	2	1.8
k_p	$10^{2.7}$	$10^{3.3}$

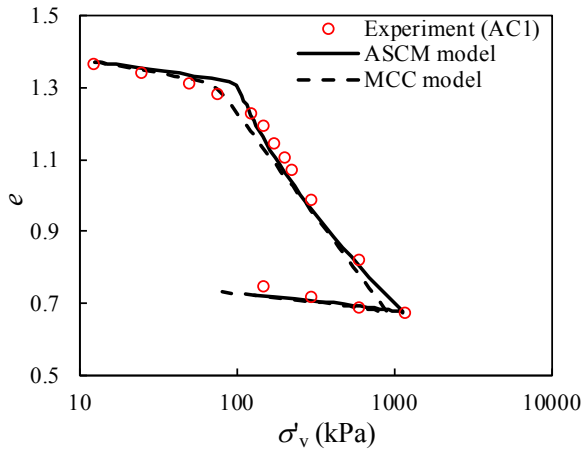

Figure 3 Simulation of oedometer test on Shanghai clay

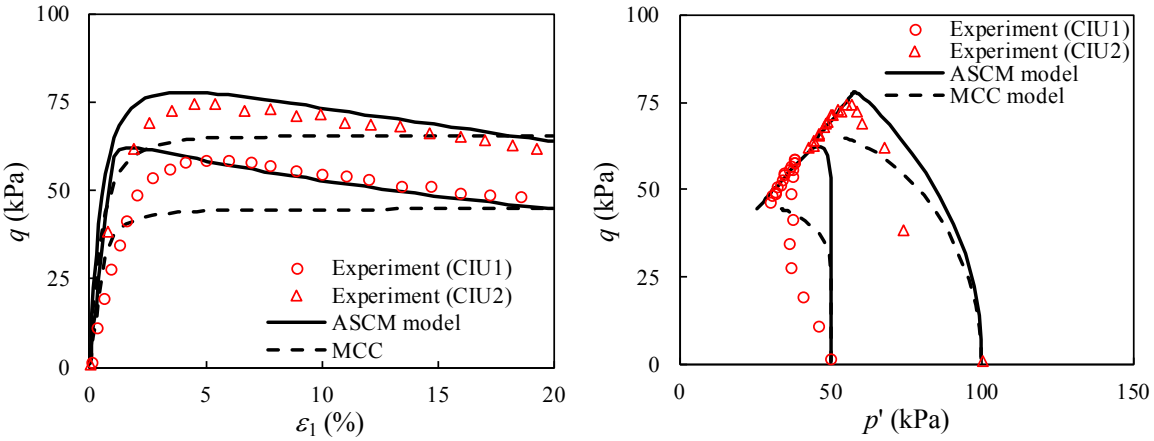

(a) deviatoric stress versus axial strain (b) deviatoric stress versus mean effective stress

Figure 4 Simulation of undrained triaxial compression tests on isotropically consolidated Shanghai clay

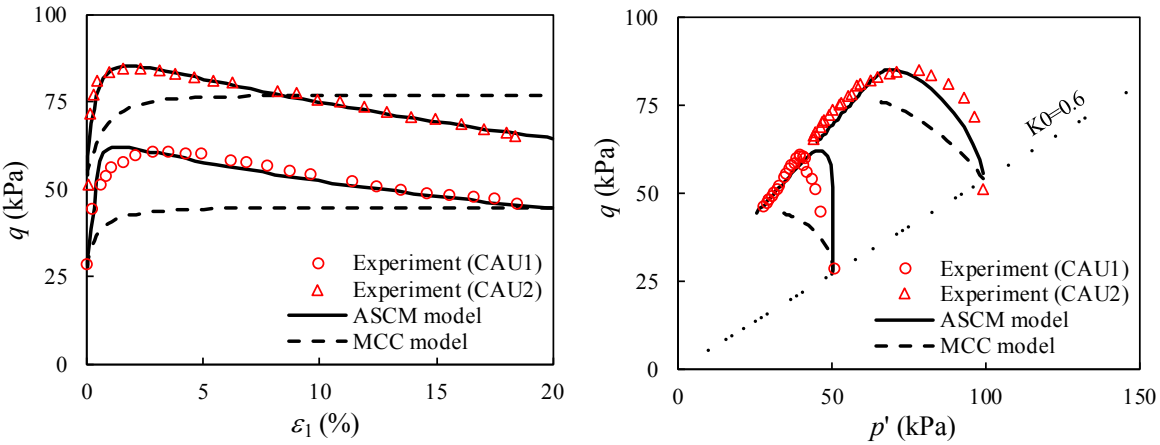

(a) deviatoric stress versus axial strain (b) deviatoric stress versus mean effective stress

Figure 5 Simulation of undrained triaxial compression tests on K_0-consolidated Shanghai clay

Numerical simulations of tests performed on samples of Vallericca stiff clay [42-44] were also undertaken. The selected triaxial tests are distinguished in two types: medium-pressure (MP) tests for values of p_0' lower than the yield stress p_{c0} and high-pressure (HP) tests where $p_0' > p_{c0}$. In all selected tests, anisotropic compression and swelling paths were applied to the natural samples before shearing. Samples were then sheared or anisotropically swelled back to different OCRs prior to shearing. Isotropic and anisotropic compression tests (see Figure 6) and one undrained triaxial test (see MP: OCR = 1 in Figure 7) were used to determine model parameters. All values of parameters are summarized in Table 1 which are used to simulate other tests on the same material.

Figure 6 shows the comparison between experimental results and simulations for the anisotropic compression test. Good agreement is achieved, as respected for parameters determination. Figure 7 shows the comparisons for all selected undrained triaxial tests with

different OCRs. In general, simulated results agree with measured ones, although discrepancies were found for some of tests which are probably due to the disturbance of intact samples. Furthermore, according to Yao et al. (2014) [45], the time-dependency not included in the proposed model may also affect the prediction performance. The model well captured the trend of destructuring behavior of stiff clay due to the destructuration process during shearing under various conditions.

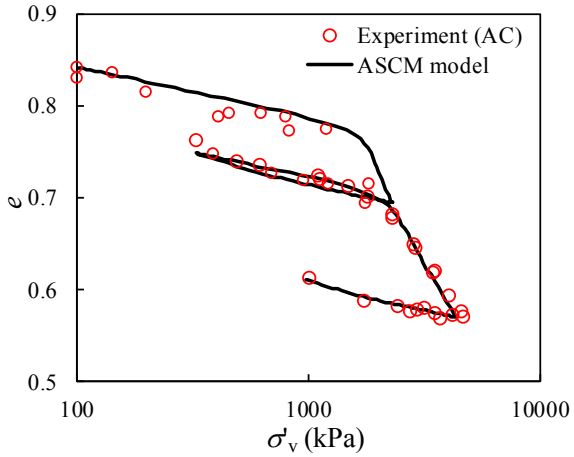

Figure 6 Simulation of oedometer test on Vallericca stiff clay

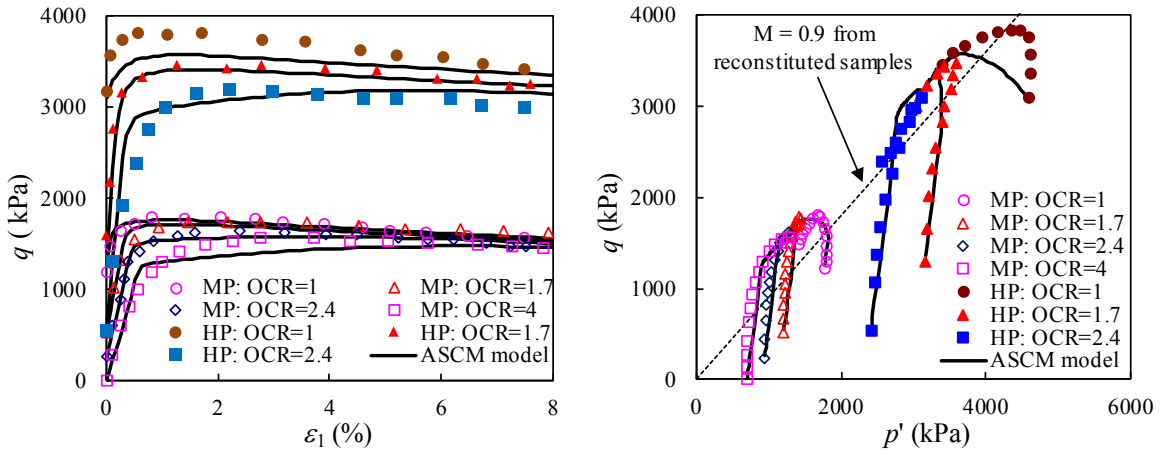

(a) deviatoric stress versus axial strain (b) deviatoric stress versus mean effective stress

Figure 7 Simulation of undrained triaxial tests on Vallericca stiff clay

Cyclic triaxial test simulations on aisotropic consolidated Shanghai clay have also been carried out. Due to the lack of experimental data on this clay, only the numerical results are presented. The material parameters for Shanghai clay, shown in Table 1, were adopted. Anisotropic compression ($K_0 = 0.6$) was applied to the sample before shearing. The cyclic simulations were performed under stress-controlled conditions, with three different amplitudes of dynamic deviatoric stress: 3 kPa, 8 kPa and 13 kPa. Figure 8 shows the accumulation of deformation during the cyclic loading and variation of stress path. As expected, the model is able to capture

the trend of the dynamic response of clay [46-48]. It is observed that with the increase of cyclic number, the accumulations of the plastic deformation keeps increasing until the failure when the stress ratio reached the critical state value 1.04.

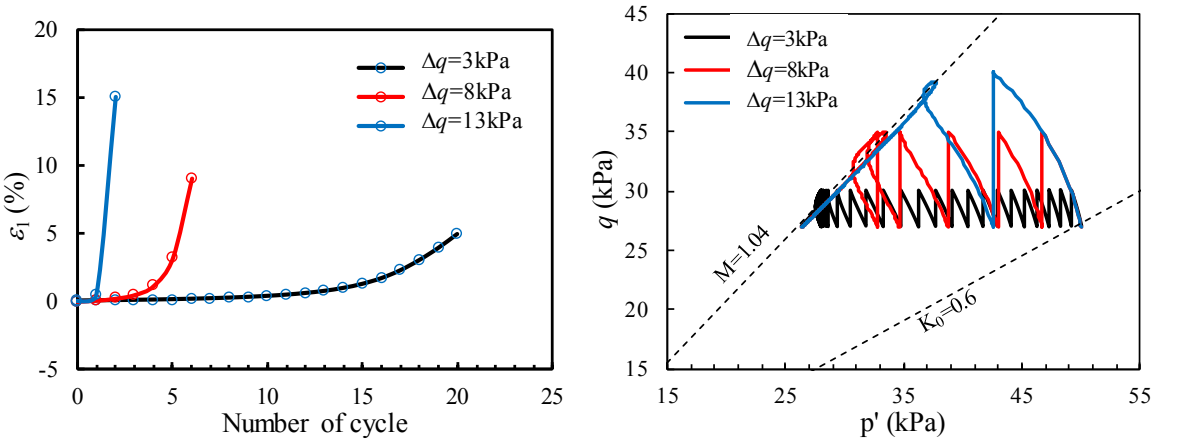

(a) axial strain versus number of cycles (b) deviatoric stress versus mean effective stress

Figure 8 Cyclic undrained triaxial test simulation

3. Model implementation via UDM in FLAC

3.1. Implementation procedure

The new constitutive model has been implemented in the commercially available finite-difference computer code FLAC2D [49], using the User-Defined Model (UDM). FLAC2D in general is one of the most popular and commonly used geotechnical analysis software worldwide. It uses an explicit time integration scheme thus the assembly of global matrices is not required. Users may implement the user-defined constitutive model for use in FLAC2D and take advantages of all modules of FLAC2D, including fluid-mechanics coupling, multi-threaded calculation, built-in free-field and quiet (viscous) boundary condition options for dynamic analysis. The above features make FLAC2D a suitable platform to apply the ASCM model, particularly for dynamics analysis.

The general calculation sequence embodied in FLAC2D is illustrated in Figure 9. This procedure first invokes the equations of motion to derive new velocities and displacements from stresses and forces. Then, strain rates are derived from velocities and new stresses from strain rates. It is the role of the UDM to accurately estimate the effective stress increment and supply an updated set of values for the state variables and the hardening parameters, given their old set of values and the applied strain increment.

The equations of motion in FLAC are integrated using the explicit central difference integration

306 rule. No global stiffness matrix is formulated with this code. Darcy's law is invoked for fluid
307 flow in a porous solid, while the incremental formulation of coupled deformation-diffusion
308 processes provides the numerical representations for the linear quasi-static Biot theory.

309 With the foregoing code, the continuum is divided into a finite difference mesh composed of
310 quadrilateral elements (or 'zones' in FLAC terminology). Mixed discretization [50] is used to
311 solve the problem of hourglassing, which may occur with constant-strain finite difference
312 quadrilaterals. Namely, each element is automatically subdivided into two overlaid sets of
313 constant-strain triangular subzones, shown in Figure 10, and stress integration is performed
314 separately for each of the four subzones of the element. However, the isotropic stress (p) and
315 strain components (ε_p) are taken to be uniform over the whole quadrilateral element and equal
316 to their average value over the four triangular sub-zones, while the deviatoric components are
317 treated separately for each triangular sub-zone. This averaging procedure of p and ε_p is
318 inherent in FLAC2D and is performed after the end of each applied strain increment. Similarly,
319 the UDM subroutine of the proposed model in FLAC introduces averaging of the hardening
320 parameters, to ensure that each quadrilateral element possesses uniform hardening parameters
321 at the end of each strain increment.

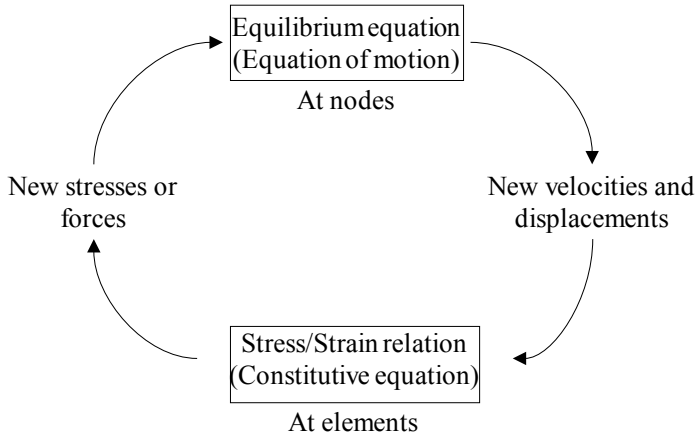

322
323 **Figure 9 Explicit calculating diagram of FLAC**

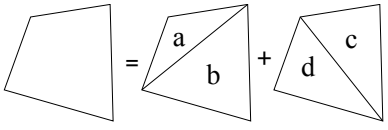

324
325 **Figure 10 Overlaid quadrilateral elements used in FLAC**

326 **3.2. Extension of cutting plane algorithm for the bounding surface model**

327 The foregoing averaging procedure is code-related and will not be elaborated further. What is
328 not code-related is the stress integration scheme employed for the new constitutive model, i.e.

the cutting plane algorithm for plastic correction, illustrated in Figure 11. The cutting plane algorithm is based on the stress surface obtained by the elastic stress trial $f\left(\sigma_i+\delta\sigma_e\right)$ as the start point and is gradually pulled back (i.e. the stress relaxation process) during the plastic correction process. In each plastic correction calculation, compared with the previous iteration result, as the plastic strain increment increases, the elastic strain increment will decrease correspondingly to ensure the total strain increment unchanged:

$$\delta\varepsilon^p=-\delta\varepsilon^e \quad (18)$$

Further derivation can obtain the amount of stress relaxation and hardening development:

$$\delta\boldsymbol{\sigma}=-\mathbf{D}\delta\varepsilon^p=-\mathbf{D}\delta\lambda\frac{\partial\bar{G}}{\partial\boldsymbol{\sigma}},\ \delta\vartheta=\frac{\partial\vartheta}{\partial\boldsymbol{\varepsilon}^p}\delta\boldsymbol{\varepsilon}^p=\frac{\partial\vartheta}{\partial\boldsymbol{\varepsilon}^p}\delta\lambda\frac{\partial\bar{G}}{\partial\boldsymbol{\sigma}},\ \delta\beta=\frac{\partial\beta}{\partial\boldsymbol{\varepsilon}^p}\delta\boldsymbol{\varepsilon}^p=\frac{\partial\beta}{\partial\boldsymbol{\varepsilon}^p}\delta\lambda\frac{\partial\bar{G}}{\partial\boldsymbol{\sigma}} \quad (19)$$

The yield function of ASCM bounding surface can be written in a compact form:

$$\bar{F}\left(\bar{\boldsymbol{\sigma}},\theta\right)=\bar{F}\left(\boldsymbol{\sigma},\theta,\beta\right) \quad (20)$$

where $\bar{\sigma}_{ij}=\beta\sigma_{ij}$, θ represents the hardening parameters.

For the plastic correction with cutting plane method, the yield equation is first-order expanded with the Taylor formula to obtain an approximate equation:

$$\bar{F}\left(\bar{\boldsymbol{\sigma}}_0+\delta\bar{\boldsymbol{\sigma}},\vartheta\right)=\bar{F}\left(\boldsymbol{\sigma}_0+\delta\boldsymbol{\sigma},\vartheta,\beta\right)=\bar{F}\left(\boldsymbol{\sigma}_0+\delta\boldsymbol{\sigma}_e,\vartheta,\beta\right)+\frac{\partial\bar{F}}{\partial\boldsymbol{\sigma}}\delta\boldsymbol{\sigma}+\frac{\partial\bar{F}}{\partial\vartheta}\delta\vartheta+\frac{\partial\bar{F}}{\partial\beta}\delta\beta=0 \quad (21)$$

The plastic loading index $\delta\lambda$ can be derived as:

$$\delta\lambda=\frac{-\bar{F}\left(\boldsymbol{\sigma}_0+\delta\boldsymbol{\sigma}_e,\vartheta,\beta\right)}{-\frac{\partial\bar{F}}{\partial\boldsymbol{\sigma}}\mathbf{D}\frac{\partial\bar{G}}{\partial\boldsymbol{\sigma}}+\frac{\partial\bar{F}}{\partial\vartheta}\frac{\partial\vartheta}{\partial\boldsymbol{\varepsilon}^p}\frac{\partial\bar{G}}{\partial\boldsymbol{\sigma}}+\frac{\partial\bar{F}}{\partial\beta}\frac{\partial\beta}{\partial\boldsymbol{\varepsilon}^p}\frac{\partial\bar{G}}{\partial\boldsymbol{\sigma}}} \quad (22)$$

According to Eq. (14) and Eq. (16), $\delta\beta$ can be derived as:

$$\delta\beta=\Phi\frac{\partial\bar{F}}{\partial\vartheta}\delta\theta \quad (23)$$

with

$$\Phi = \frac{\beta - \frac{\bar{K}_p}{K_p}}{\left(\frac{\partial \bar{F}}{\partial \bar{s}_{ij}} s_{ij} + \frac{\partial \bar{F}}{\partial \bar{p}'} p'\right)\beta + \left(\frac{\bar{K}_p}{K_p} - \beta\right)\frac{\partial \bar{F}}{\partial \beta}} \quad \text{.....(24)}$$

Then Eq. (22) becomes:

$$\delta\lambda = \frac{-\bar{F}\left(\boldsymbol{\sigma}_0 + \delta\boldsymbol{\sigma}_e, \vartheta, \beta\right)}{-\frac{\partial \bar{F}}{\partial \boldsymbol{\sigma}} \mathbf{D} \frac{\partial \bar{G}}{\partial \boldsymbol{\sigma}} + \left(1 + \Phi \frac{\partial \bar{F}}{\partial \beta}\right)\frac{\partial \bar{F}}{\partial \vartheta}\frac{\partial \vartheta}{\partial \boldsymbol{\varepsilon}^p}\frac{\partial \bar{G}}{\partial \boldsymbol{\sigma}}} \quad \text{.....(25)}$$

According to Eq. (16) and Eq. (19):

$$\frac{\partial \bar{F}}{\partial \vartheta}\frac{\partial \vartheta}{\partial \varepsilon^p}\frac{\partial \bar{G}}{\partial \boldsymbol{\sigma}} = \frac{\partial \bar{F}}{\partial \vartheta}\frac{\partial \vartheta}{\partial \varepsilon^p}\left(\beta \frac{\partial \bar{G}}{\partial \bar{\boldsymbol{\sigma}}}\right) = \beta \bar{K}_p \quad \text{.....(26)}$$

By substituting Eqs. (17), (24) and (26) into Eq. (25), $\delta\lambda$ can be derived as

$$\delta\lambda = \frac{-\bar{F}\left(\boldsymbol{\sigma}_0 + \delta\boldsymbol{\sigma}_e, \vartheta, \beta\right)}{-hh + dd} \quad \text{.....(27)}$$

with

$$hh = \frac{\partial \bar{F}}{\partial \boldsymbol{\sigma}} D \frac{\partial \bar{G}}{\partial \boldsymbol{\sigma}}$$

$$dd = \left(1 + \Phi \frac{\partial \bar{F}}{\partial \beta}\right)\beta\left[\frac{1}{\beta^2}\frac{\partial \bar{F}}{\partial \vartheta}\frac{\partial \vartheta}{\partial \varepsilon^p}\frac{\partial \bar{G}}{\partial \bar{\boldsymbol{\sigma}}} - \frac{k_p}{c_p}\left(\beta p'\right)^3\left(1 - \frac{1}{\beta}\right)\right] \quad \text{.....(A28)}$$

The stress, hardening parameters and the mapping coefficient after the plastic correction can then be obtained by:

$$\begin{aligned}
\boldsymbol{\sigma}_{i+1}^{j+1} &= \boldsymbol{\sigma}_{i+1}^{j} - D\delta\lambda\frac{\partial \bar{G}}{\partial \boldsymbol{\sigma}} \\
\vartheta_{i+1}^{j+1} &= \vartheta_{i+1}^{j} + \frac{\partial \vartheta}{\partial \boldsymbol{\varepsilon}^p}\delta\lambda\frac{\partial \bar{G}}{\partial \boldsymbol{\sigma}} \quad \text{.....(29)} \\
\beta_{i+1}^{j+1} &= \beta_{i+1}^{j} + \frac{\partial \beta}{\partial \boldsymbol{\varepsilon}^p}\delta\lambda\frac{\partial \bar{G}}{\partial \boldsymbol{\sigma}}
\end{aligned}$$

where $(i+1)$ represents the current increment, j represents the iteration number of the current increment. If the convergence condition $\bar{F}\left(\boldsymbol{\sigma}_{i+1}^{j+1}, \vartheta_{i+1}^{j+1}, \beta_{i+1}^{j+1}\right) <$ tolerance is not satisfied at this time, the plastic correction calculation will continue according to Eqs. (18) - (29) until the convergence. The flowchart for implementing the proposed bounding surface model by cutting

plane algorithm is presented in Figure 12. The deviations of yield function can be found in the Appendix.

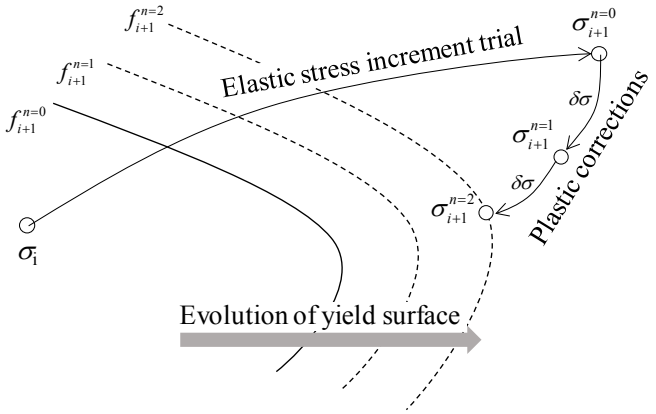

Figure 11 Illustration of the correction phase of cutting plane algorithm for plasticity

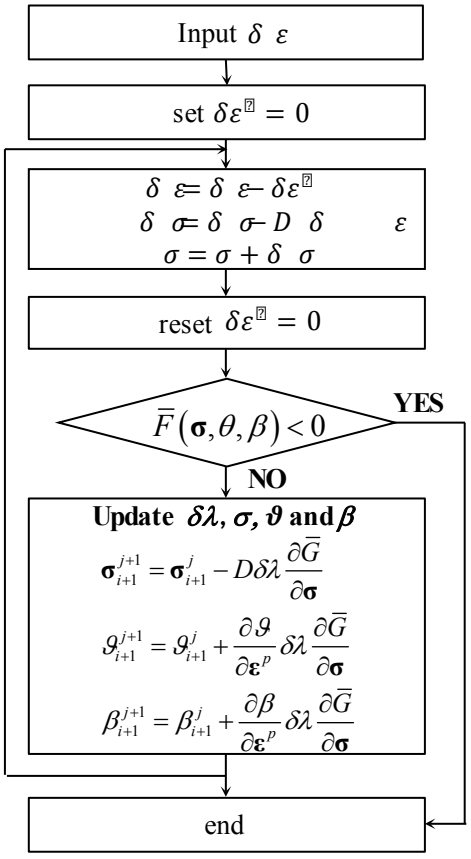

Figure 12 flowchart for implementing the ASCM model by cutting plane algorithm

4. Analysis of load transfer in clay foundation due to metro operation

4.1. Description of the problem

4.1.1. Geometry

A sketch of the investigated tunnel is provided in Figure 13, based on a typical shield tunnel in Shanghai [51]. The cross-section of the tunnel is assumed to be circular. The external and

internal diameters of the shield tunnel are 6.2m and 5.5m, respectively, and the thickness of the concrete segment is 0.35 m. The tunnel is constructed at a depth of 10.5m from the ground surface to the top of the tunnel. The problem is analysed under the assumption of a plane strain condition. The 2D finite difference elements and the liner elements were used to represent the soil and the tunnel lining respectively. The specified mesh and boundary conditions are shown in Figure 14. The viscous boundary conditions are used to eliminate wave reflections (dynamic effect) at model boundaries. Considering the symmetric condition and the calculation efficiency of the user defined model in FLAC, only the right half of the specific domain is modelled with a relatively coarse mesh. The model extended 30 m in width and 35 m in height. The lateral displacement boundaries were fixed in the horizontal direction but allowed to move vertically, and the displacement boundary at the bottom was fixed in both horizontal and vertical directions.

However, it should be noted that the present work is a theoretical study. The aim is to develop an accurate dynamic constitutive model and apply it in analyzing the role of soil properties to the load transfer in clay foundation due to the traffic load. Since the focus is not upon a comparison with a real case, a relative coarse mesh was used in the simulation to save the calculation cost of the coupled hydromechanical dynamic analysis. The numerical results were analyzed in a rather qualitive way.

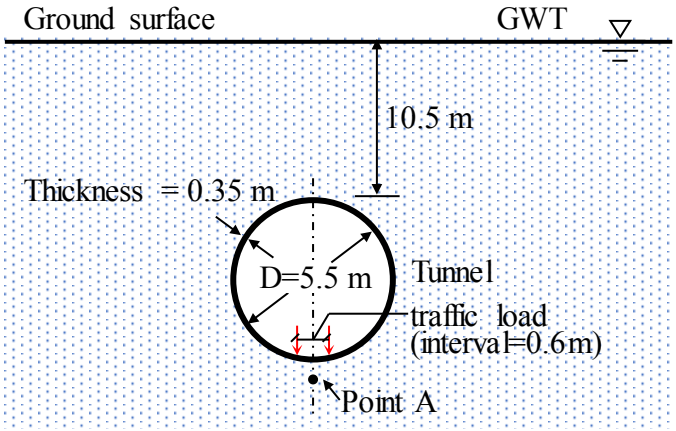

Figure 13 Problem geometry used in the numerical analysis

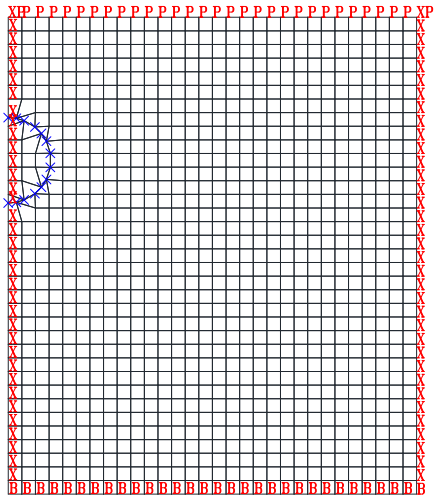

Figure 14 Mesh of model

4.1.2. Initial stress

The groundwater level is considered to be at the ground surface. The corresponding initial pore pressure is set up accordingly in the whole domain. Effective stresses are initialized within the soil, due to its self-weight. The coefficient of earth pressure at rest, K_0, is assumed as equal to 0.5. The excavation of the tunnel and the installation of the linings are simulated in order to generate the initial stress before applying the vibration loads. The settlements caused by tunnelling are often characterized by the term "ground loss," expressed as a percentage of the notional excavated volume of the tunnel. In this study, the ratio of ground loss during tunnel construction is assumed to be 2% [52].

4.1.3. Model parameters

The tunnel lining was made of precast reinforced concrete, and the linear elastic model was used for the tunnel lining. As the joints between the segments reduced the tunnel stiffness significantly, the jointed segmental tunnel lining was simulated using the method of continuous solid elements with reduced stiffness ([53-55]). Accordingly, the Young's modulus of the linear elastic elements of lining is 30 GPa, and the Poisson's ratio is 0.2.

The ASCM model with the parameters corresponding to the Shanghai soft clay (shown in Table 1) is adopted for soil elements. The initial void ratio and POP are 1.37 and 24.6 kPa respectively.

4.1.4. Train vibration load

The exciting force caused by the geometric irregularity of the train and the tracks can be simulated by an exciting force function [56] as follow:

$$F(t) = P_0 + \mathrm{P}_1 \sin(\omega_1 t) + P_2 \sin(\omega_2 t) + P_3 \sin(\omega_3 t) \quad \text{.....(30)}$$

where P_0 is the static wheel load; P_1, P_2 and P_3 are the amplitudes of dynamic wheel load corresponding to the high, medium and small angular frequency ω_i :

$$P_i = M_0 \alpha_i \omega_i^2,\ \omega_i = 2\pi v / L_i,\ i = 1,2,3 \quad \text{.....(31)}$$

where M_0 is the mass of the train; α_i and L_i are the versine and wavelength of the corresponding dynamic load, v is the train velocity. The typical values of the dynamic loads and the corresponding angular frequency are given in Table 2. The exciting force curve is shown in Figure 15.

Table 2 dynamic loads

$\boldsymbol{P_0}$ /kN	v m/s	$\boldsymbol{L_1}$/m	$\boldsymbol{L_2}$/m	$\boldsymbol{L_3}$/m	$\boldsymbol{\alpha_1}$/mm	$\boldsymbol{\alpha_2}$/mm	$\boldsymbol{\alpha_3}$/mm
17.39	20	10	2	0.5	3.5	0.4	0.08
$\boldsymbol{M_0}$ /kg		$\boldsymbol{\omega_1}$	$\boldsymbol{\omega_2}$	$\boldsymbol{\omega_3}$	$\boldsymbol{P_1}$	$\boldsymbol{P_2}$	$\boldsymbol{P_3}$
1738.56		12.57	62.83	251.32	0.96	2.75	8.79

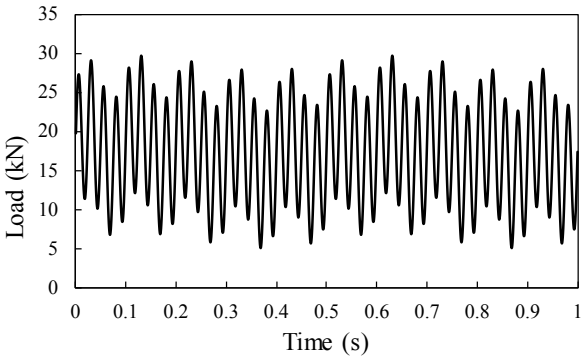

Figure 15 Train vibration load

4.1.5. Simulated cases

A set of parametric studies have been carried out to characterize the influencing factors of the load transfer in the clay foundation due to the traffic load of the metro tunnel. The simulated cases are organized as follows:

In section 4.2.1, the role of the dynamic constitutive model is highlighted by comparing the results of a static constitutive model (MCC model) and a dynamic constitutive model (isotropic ASCM model, equivalent to MCC bounding surface model). The anisotropy and the structure of nature clay are not considered in the isotropic ASCM model. The critical state-related parameters for both MCC model and the isotropic ASCM model are shown in Table 1. It should be noted that for the isotropic ASCM model, k_p is the shape parameter of the bounding surface

440 model. With an increasing k_p, the isotropic ASCM model should approach the MCC model.
441 Therefore, two simulations are carried out using the isotropic ASCM model, with $k_p = 10^{2.7}$
442 and $k_p = 10^4$ respectively, to illustrate the transition of a dynamic constitutive model to a static
443 model when k_p increases.

444 In section 4.2.2, three additional simulations have been carried out to analyse the influence of
445 the anisotropy, the structure ratio and the adhesive mean stress of soil on the load transfer in
446 clay: (1) with the anisotropic ASCM model (equivalent to S-CLAY1 model [24]), the structure
447 of nature clay is not considered; (2) with the anisotropic ASCM model considering the structure
448 ratio (χ) and (3) with the anisotropic ASCM model considering the structure ratio (χ) and
449 adhesive mean stress (p_b) of undisturbed nature clay. The model parameters are shown in
450 Table 1.

451 **4.2. Numerical results and discussions**

452 *4.2.1. Comparison between the static and dynamic constitutive model*

453 Figure 17 shows the time variation of the dynamic stresses and excess pore water pressure at
454 2m below the tunnel (point A, shown in Figure 13), generated by the trainload under a single
455 train operation (Time=10s).

456 For the case with the dynamic constitutive model (isotropic ASCM model), the vertical and
457 horizontal dynamic stress, as well as the excess pore pressure increase gradually. Meanwhile,
458 for the case with the static constitutive model (MCC model), as there is no accumulation of
459 plastic deformation in the soil beneath the tunnel, the dynamic vertical and horizontal stress
460 and the excess pore water pressure keep constant after the transient increase.

461 Figure 16 shows the time variation of ground surface settlement above the centre of the tunnel
462 during a single train operation. It can be seen that due to the accumulation of plastic
463 deformation, the settlement obtained by using the dynamic constitutive model increases
464 gradually. At the end of 10s, the maximum surface settlement was 2.5 cm, which was
465 significantly greater than that obtained by using the static constitutive model, which was 0.5cm.

466 At the same time, it can be seen that with a larger k_p, the results of the dynamic constitutive
467 model (isotropic ASCM model) are approaching the results of the static constitutive model
468 (MCC model). The excess pore pressure at the end of 10s decreased from 14.1 kPa to 5.17 kPa

when k_p increased form $10^{2.7}$ to 10^4. It is reasonable to expect that the excess pore pressure at the end of 10s will reach the value obtained by the static MCC model when k_p is large enough. The same trend could be found for the vertical and horizontal dynamic stress, as well as the ground surface settlement.

Figure 18 shows the spatial distribution of excess pore pressure after a single train operation. For the static and dynamic constitutive model, the max excess pore pressures are respectively 2.9 kPa and 18.45 kPa, at the bottom of the tunnel. With an increase of distance from the tunnel, the excess pore pressures decrease gradually. For the case with the dynamic constitutive model, the reduction of excess pore pressures is significant in the shallow subsoil.

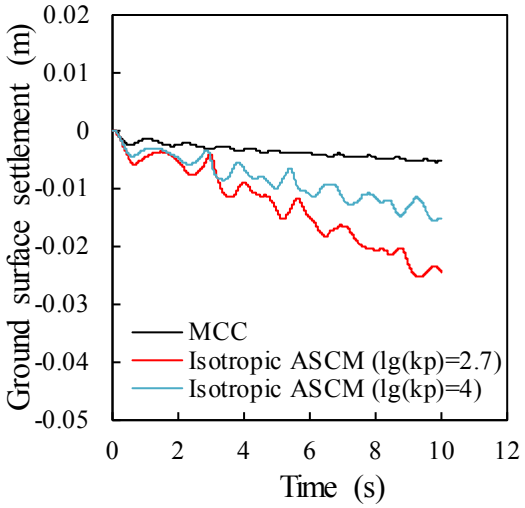

Figure 16 Time variation of ground settlement

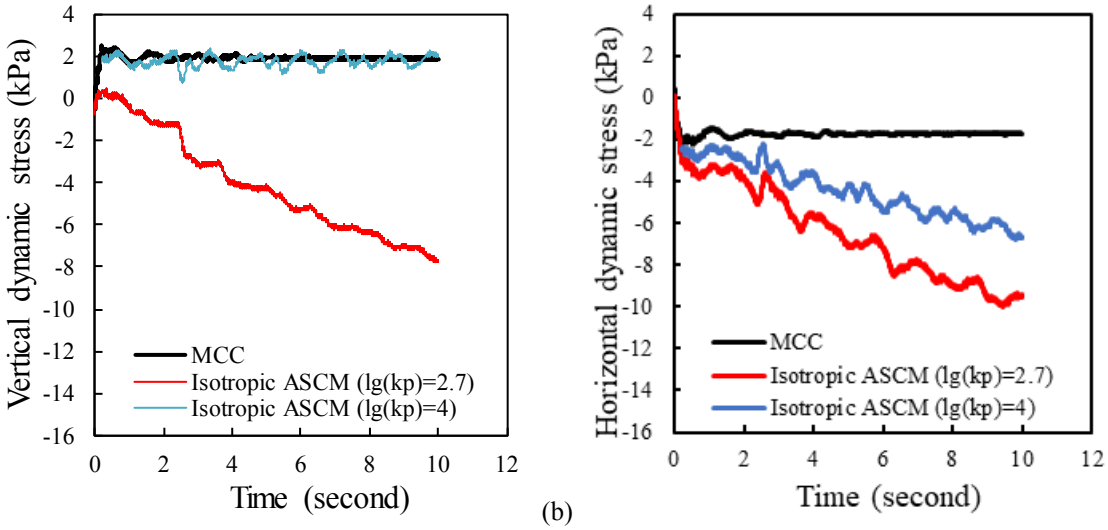

(a) (b)

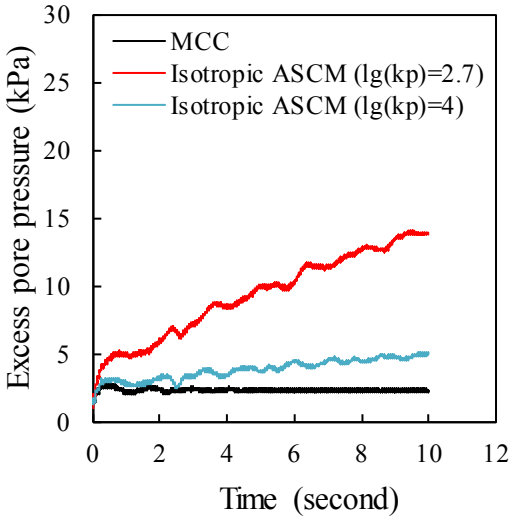

(c)

Figure 17 Time variation of the stresses at 2m below the tunnel

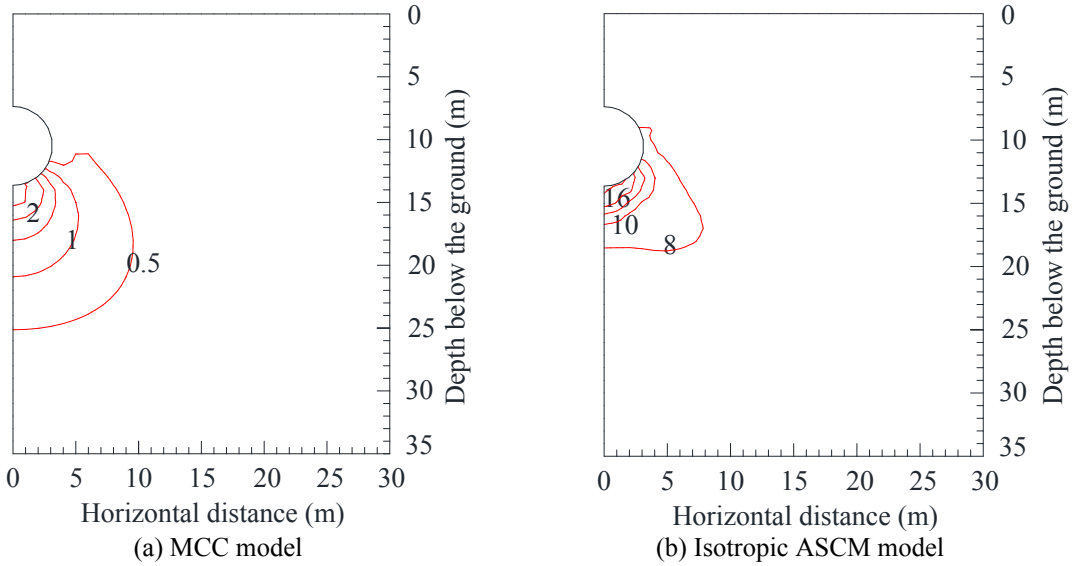

(a) MCC model (b) Isotropic ASCM model

Figure 18 Spatial distribution of excess pore pressure at Time=10s

4.2.2. Influences of the anisotropy and the soil structure on the load transfer in clay

Three additional simulations have been carried out to analyse the influence of the anisotropy, the structure ratio (χ) and the adhesive mean stress (p_b) of soil on the load transfer in clay foundation due to the traffic load of the metro tunnel. Figure 19 shows the time variation of the dynamic stresses and excess pore water pressure at 2m below the tunnel, generated by the trainload under a single train operation (Time=10s). Figure 20 shows the time variation of ground surface settlement above the centre of the tunnel caused by a single train operation. It is obvious that the anisotropy and the structure of soil have a significant effect on the dynamic response of the soil.

Compared to the isotropic ASCM model, the introduction of anisotropy decreases the dynamic

stress and excess pore pressure. When the initial anisotropy of the soil increases, the symmetry axis of the initial yield surface gradually changes from the hydrostatic axis to the K_0 line, leading to an increase of its peak shear strength. As a result, the corresponding variation of the mean effective stress, as well as the excess pore pressure, decrease. The introduction of χ and p_b indicates that the soil is structural. The scalar variable χ controls the ratio between the sizes of the structure surface and reference surface. The degradation of the structural surface induced by the dynamic load makes the soil "softer", leading to an increase of the variation of the mean effective stress and that of the excess pore pressure. However, the presence of the adhensive mean stress p_b makes it more difficult to reache the structural yield stress. When the external force does not reach the structural yield stress, the soil exhibits higher stiffness. As a result, the ground settlement is the smallest for the case when the anisotropy and the structure (χ, p_b) of the soil are considered.

Figure 21 shows the spatial distribution of excess pore pressure after a single train operation. For all the cases, with an increase of distance from the tunnel, the excess pore pressure decreases gradually. Compared with the isotropic ASCM model, the introduction of soil's anisotropy reduces the excess pore water pressure below the tunnel; the introduction of structure ratio χ increases the excess pore water pressure. However, when the adhesive mean stress p_b is considered, the excess pore water pressure below the tunnel is significantly reduced. This can be explained by the fact that the consideration of p_b will increase the peak shear strength and initial stiffness of the soil.

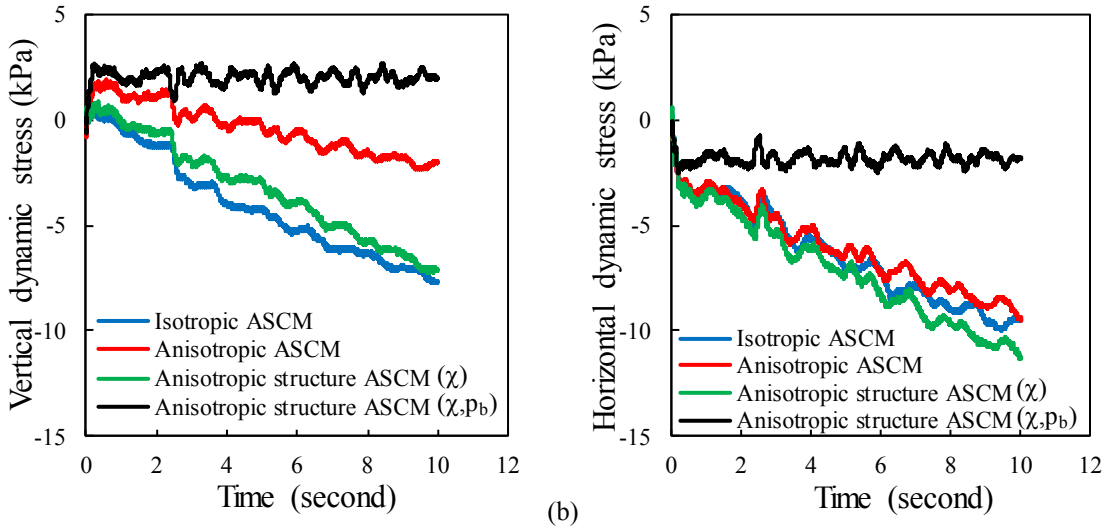

(a) (b)

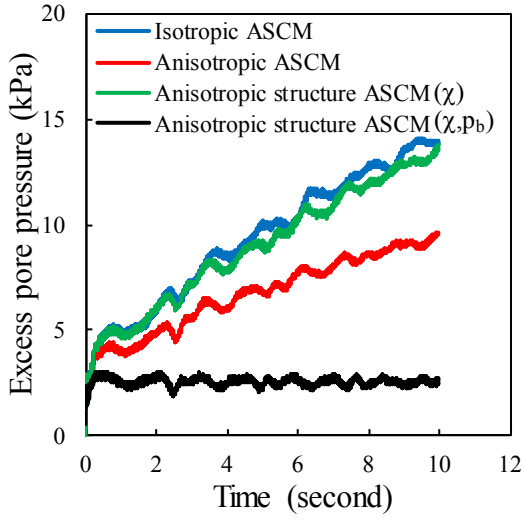

(c)

Figure 19 Time variation the vertical and horizontal stresses and the excess pore pressure below the tunnel

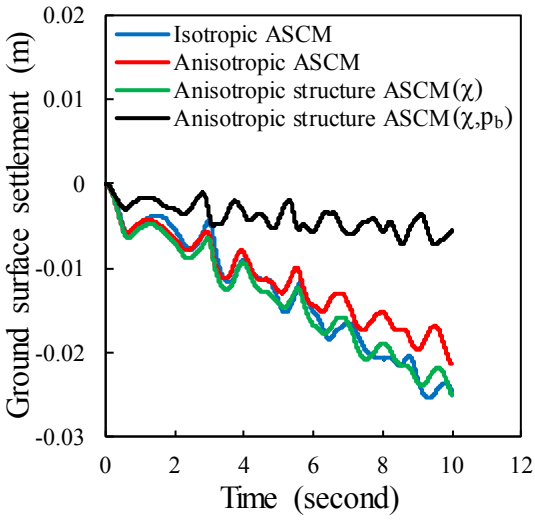

Figure 20 Time variation of ground settlement

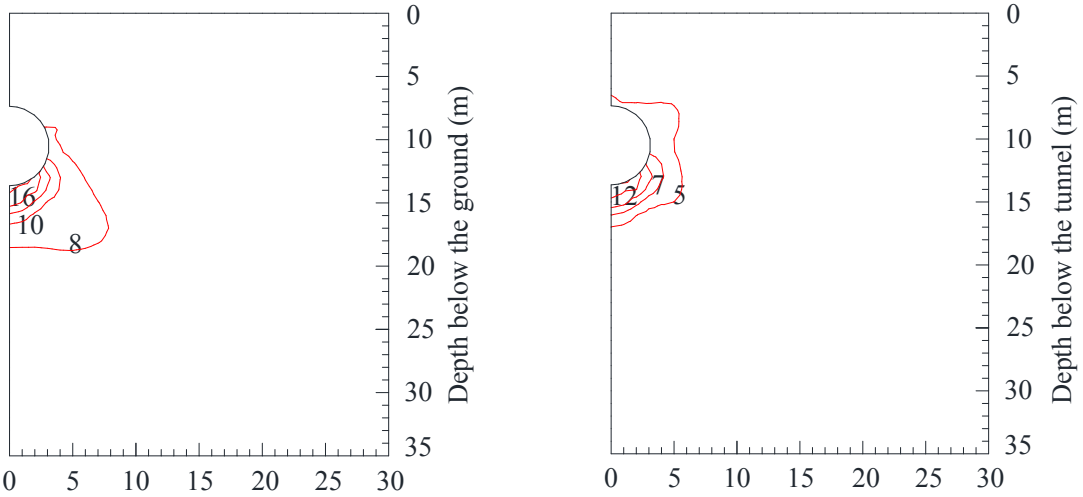

(a) Isotropic ASCM model

(b) Anisotropic ASCM model

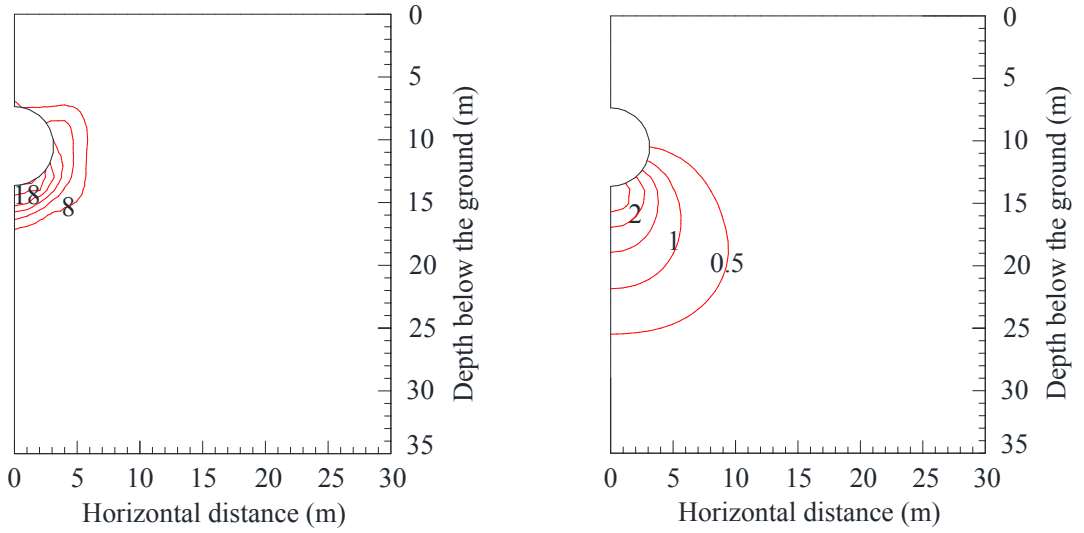

524
525 (c) Anisotropic structure ASCM model (χ) (d) Anisotropic structure ASCM model (χ , p_b)

526 **Figure 21 Spatial distribution of excess pore pressure at Time=10s**

527 ## 5. Conclusions

528 A new critical state based bounding surface model for natural structured clays have been
529 developed to investigate the traffic load transfer in clay foundation of metro tunnel. This model
530 is able to consider the initial and induced anisotropy of nature clay and the structure disturbance
531 to the initial size of yield surface and to the initial adhesive stress by cyclic loading at low-
532 stress levels. Odeometer tests and undrained triaxial tests on Shanghai clay and Vallericca stiff
533 clay were simulated to evaluate the proposed model. Comparisons between experimental
534 results and simulations demonstrate a good predictive ability of the proposed model.

535 The ASCM model was implemented into FLAC2D as a user-defined model to couple with the
536 Biot's consolidation theory. The the ASCM model in FLAC2D was then applied to simulate
537 the dynamic responses of the metro tunnel due to the train vibration load. It is observed that
538 the static constitutive model is not able to reproduce the accumulation of plastic deformation
539 and the excess pore water pressure under the traffic loads of the metro tunnel. Meanwhile,
540 when the dynamic constitutive model (Isotropic ASCM here) was used, the vertical and
541 horizontal dynamic stress, as well as the excess pore pressure increase gradually during the
542 metro operation. At the same time, due to the accumulation of plastic deformation, the
543 settlement obtained by using the dynamic constitutive model continues to increase.

544 Furthermore, the anisotropy and the structure of nature clay have a significant effect on the
545 dynamic response of the soil to the traffic loads of the metro tunnel, which should be both
546 considered in the engineering practice. Compared to the isotropic ASCM model, the

introduction of clay's anisotropy or adhesive mean stress may decrease the dynamic stress and the excess pore pressure while the introduction of clay's structure ratio χ may lead to the increase of the dynamic stress and the excess pore pressure. Meanwhile, more attention should be paid to the degradation of the clay's structure ratio χ, without which the dynamic stress and the excess pore pressure induced by the traffic loads of the metro tunnel could be underestimated.

It is worth mentioning that the present work is a theoretical study to investigate the role of soil properties to the load transfer in clay foundation induced by the traffic load. In the future case study, with simple empirical or analytical models describing the permanent strain or/and pore water pressure with the number of cycles, the developed dynamic constitutive model can be applied to assess more accurately the long-term behaviors of tunnel due to the traffic load.

Acknowledgment

The financial support provided by the GRF project (Grant No. 15209119) from the Research Grants Council (RGC) of Hong Kong, Joint research project between SiChuan Province and National Universities funded by Science & Technology Department of Sichuan Province (No.2019YFSY0015), and Open research grant of MOE Key Laboratory of High-speed Railway Engineering are gratefully acknowledged.

Appendix: Some derivatives of yield function

$$\frac{\partial \bar{F}}{\partial \bar{s}_{ij}} = \frac{3\left[\beta s_{ij} - \left(\beta p' + p_b\right)\alpha_{ij}\right]}{\left(M^2 - \frac{3}{2}\alpha_{ij} : \alpha_{ij}\right)} \quad \text{.....(A33)}$$

$$\frac{\partial \bar{F}}{\partial \bar{p}'} = \frac{-3\left[\beta s_{ij} - \left(\beta p' + p_b\right)\alpha_{ij}\right] : \alpha_{ij}}{\left(M^2 - \frac{3}{2}\alpha_{ij} : \alpha_{ij}\right)} + 2\beta p' - \left(1+\chi\right)p_{ci} + p_b \quad \text{.....(A34)}$$

$$\frac{\partial \bar{F}}{\partial \beta} = \frac{3\left[\beta s_{ij} - \left(\beta p' + p_b\right)\alpha_{ij}\right] : \left(s_{ij} - p'\alpha_{ij}\right)}{\left(M^2 - \frac{3}{2}\alpha_{ij} : \alpha_{ij}\right)} + 2\beta p'^2 - p'\left(1+\chi\right)p_{ci} + p'p_b \quad \text{.....(A35)}$$

570 $$\frac{\partial \bar{F}}{\partial \vartheta_1(p_b)} = \frac{-3\left[\beta s_{ij} - (\beta p' + p_b)\alpha_{ij}\right] : \alpha_{ij}}{\left(M^2 - \frac{3}{2}\alpha_{ij} : \alpha_{ij}\right)} + \beta p' - (1+\chi)\, p_{ci} \quad \text{.....(A36)}$$

571 $$\frac{\partial \bar{F}}{\partial \vartheta_2(\alpha_{ij})} = \frac{-3\left[\beta s_{ij} - (\beta p' + p_b)\alpha_{ij}\right](\beta p' + p_b)}{\left(M^2 - \frac{3}{2}\alpha_{ij} : \alpha_{ij}\right)} + \frac{9\left[\left(\beta s_{ij} - (\beta p' + p_b)\alpha_{ij}\right) : \left(\beta s_{ij} - (\beta p' + p_b)\alpha_{ij}\right)\right]\alpha_{ij}}{2\left(M^2 - \frac{3}{2}\alpha_{ij} : \alpha_{ij}\right)^2} \quad \text{.....(A37)}$$

572 $$\frac{\partial \bar{F}}{\partial \vartheta_3(\chi)} = -(\beta p' + p_b)\, p_{ci} \quad \text{.....(A38)}$$

573 $$\frac{\partial \bar{F}}{\partial \vartheta_4(p_{ci})} = -(\beta p' + p_b)(1+\chi) \quad \text{.....(A39)}$$

574

References

[1] Shen S-L, Wu H-N, Cui Y-J, Yin Z-Y. Long-term settlement behaviour of metro tunnels in the soft deposits of Shanghai. Tunnelling Underground Space Technol. 2014;40:309-323.

[2] Wu H-N, Shen S-L, Yang J. Identification of tunnel settlement caused by land subsidence in soft deposit of Shanghai. Journal of Performance of Constructed Facilities. 2017;31:04017092.

[3] Lee K, Ji H, Shen C, Liu J, Bai T. Ground response to the construction of Shanghai metro tunnel-line 2. Soils Found. 1999;39:113-134.

[4] Ren D-J, Shen S-L, Arulrajah A, Wu H-N. Evaluation of ground loss ratio with moving trajectories induced in double-O-tube (DOT) tunnelling. Can Geotech J. 2017;55:894-902.

[5] Liu XX, Shen SL, Xu YS, Yin ZY. Analytical approach for time‐dependent groundwater inflow into shield tunnel face in confined aquifer. Int J Numer Anal Methods Geomech. 2018;42:655-673.

[6] Tang Y-Q, Cui Z-D, Zhang X, Zhao S-K. Dynamic response and pore pressure model of the saturated soft clay around the tunnel under vibration loading of Shanghai subway. Engineering Geology. 2008;98:126-132.

[7] Brown S, Lashine A, Hyde A. Repeated load triaxial testing of a silty clay. Geotechnique. 1975;25:95-114.

[8] Kampala A, Horpibulsuk S, Chinkullijniwat A, Shen S-L. Engineering properties of recycled calcium carbide residue stabilized clay as fill and pavement materials. Construction and Building Materials. 2013;46:203-210.

[9] Lee KL, Focht Jr JA. Strength of clay subjected to cyclic loading. Mar Georesour Geotechnol. 1976;1:165-185.

[10] Sangrey D, Henkel D, Esrig MI. The effective stress response of a saturated clay soil to repeated loading. Can Geotech J. 1969;6:241-252.

[11] Yasuhara K, Yamanouchi T, HIRAO K. Cyclic strength and deformation of normally consolidated clay. Soils Found. 1982;22:77-91.

[12] Chai J-C, Miura N. Traffic-load-induced permanent deformation of road on soft subsoil. J Geotech Geoenviron Eng. 2002;128:907-916.

[13] Li D, Selig ET. Cumulative plastic deformation for fine-grained subgrade soils. Journal of geotechnical engineering. 1996;122:1006-1013.

[14] Lu J-F, Jeng D-S. Dynamic response of a circular tunnel embedded in a saturated poroelastic medium due to a moving load. Journal of vibration and acoustics. 2006;128:750-756.

[15] Chen Z, Hong-lei S, Yuan-qiang C, Zhi-gang C. Dynamic response of lined tunnel in saturated soil due to moving load. Journal of Zhejiang University (Engineering Science). 2015;49:511-521.

[16] Yuan Z, Cai Y, Cao Z. An analytical model for vibration prediction of a tunnel embedded in a saturated full-space to a harmonic point load. Soil Dynamics and Earthquake Engineering. 2016;86:25-40.

[17] Yuan Z, Xu C, Cai Y, Cao Z. Dynamic response of a tunnel buried in a saturated poroelastic soil layer to a moving point load. Soil Dynamics and Earthquake Engineering. 2015;77:348-359.

[18] Huang Q, Huang H-w, Ye B, Zhang D-m, Gu L-l, Zhang F. Dynamic response and long-term settlement of a metro tunnel in saturated clay due to moving train load. Soils Found. 2017;57:1059-1075.

[19] Huang Q, Huang H, Ye B, Zhang D, Zhang F. Evaluation of train-induced settlement for metro tunnel in saturated clay based on an elastoplastic constitutive model. Underground Space. 2018;3:109-124.

624 [20] Li D, Selig ET. Method for railroad track foundation design. II: Applications. J Geotech
625 Geoenviron Eng. 1998;124:323-329.
626 [21] Wu H-N, Shen S-L, Chai J-C, Zhang D-M, Xu Y-S. Evaluation of train-load-induced
627 settlement in metro tunnels. Proceedings of the Institution of Civil Engineers-Geotechnical
628 Engineering. 2014;168:396-406.
629 [22] Roscoe KH, Burland J. On the generalized stress-strain behaviour of wet clay. 1968.
630 [23] Dafalias YF. Bounding Surface Plasticity. I: Mathematical Foundation and
631 Hypoplasticity. J Eng Mech. 1986;112:966-987.
632 [24] Wheeler SJ, Näätänen A, Karstunen M, Lojander M. An anisotropic elastoplastic model
633 for soft clays. Can Geotech J. 2003;40:403-418.
634 [25] Sheng D, Sloan SW, Yu HS. Aspects of finite element implementation of critical state
635 models. Computational Mechanics. 2000;26:185-196.
636 [26] Yao YP, Sun DA, Matsuoka H. A unified constitutive model for both clay and sand with
637 hardening parameter independent on stress path. Comput Geotech. 2008;35:210-222.
638 [27] Yao Y-P, Hou W, Zhou A-N. UH model: three-dimensional unified hardening model for
639 overconsolidated clays. Géotechnique. 2009;59:451-469.
640 [28] Yin Z-Y, Karstunen M. Modelling strain-rate-dependency of natural soft clays combined
641 with anisotropy and destructuration. Acta Mechanica Solida Sinica. 2011;24:216-230.
642 [29] Yin Z-Y, Chang CS, Karstunen M, Hicher P-Y. An anisotropic elastic–viscoplastic model
643 for soft clays. Int J Solids Struct. 2010;47:665-677.
644 [30] Yin Z-Y, Karstunen M, Chang CS, Koskinen M, Lojander M. Modeling time-dependent
645 behavior of soft sensitive clay. J Geotech Geoenviron Eng. 2011;137:1103-1113.
646 [31] Karstunen M, Yin Z-Y. Modelling time-dependent behaviour of Murro test embankment.
647 Géotechnique. 2010;60:735-749.
648 [32] Abdoulaye Hama N, Ouahbi T, Taibi S, Souli H, Fleureau JM, Pantet A. Analysis of
649 mechanical behaviour and internal stability of granular materials using discrete element
650 method. Int J Numer Anal Methods Geomech. 2016;40:1712-1729.
651 [33] Yin ZY, Hattab M, Hicher PY. Multiscale modeling of a sensitive marine clay. Int J Numer
652 Anal Methods Geomech. 2011;35:1682-1702.
653 [34] Dafalias Y. Bounding surface formulation of soil plasticity. Soil mechanics-transient and
654 cyclic loads. 1982:253-282.
655 [35] Jin Y-F, Yin Z-Y, Zhou W-H, Huang H-W. Multi-objective optimization-based updating
656 of predictions during excavation. Engineering Applications of Artificial Intelligence.
657 2019;78:102-123.
658 [36] Yin ZY, Jin YF, Shen JS, Hicher PY. Optimization techniques for identifying soil
659 parameters in geotechnical engineering: Comparative study and enhancement. Int J Numer
660 Anal Methods Geomech. 2018;42:70-94.
661 [37] Yin Z-Y, Jin Y-F, Shen S-L, Huang H-W. An efficient optimization method for identifying
662 parameters of soft structured clay by an enhanced genetic algorithm and elastic–viscoplastic
663 model. Acta Geotech. 2016:1-19.
664 [38] Jin YF, Yin ZY, Shen SL, Hicher PY. Selection of sand models and identification of
665 parameters using an enhanced genetic algorithm. Int J Numer Anal Methods Geomech.
666 2016;40:1219-1240.
667 [39] Jin YF, Yin ZY, Zhou WH, Shao JF. Bayesian model selection for sand with
668 generalization ability evaluation. Int J Numer Anal Methods Geomech. 2019.
669 [40] Jin Y-F, Yin Z-Y, Zhou W-H, Horpibulsuk S. Identifying parameters of advanced soil
670 models using an enhanced transitional Markov chain Monte Carlo method. Acta Geotech.
671 2019;14:1925-1947.
672 [41] Huang M, Liu Y, Sheng D. Simulation of yielding and stress–stain behavior of shanghai
673 soft clay. Comput Geotech. 2011;38:341-353.

[42] Amorosi A, Rampello S. An experimental investigation into the mechanical behaviour of a structured stiff clay. Géotechnique. 2007;57:153-166.
[43] Rampello S, Georgiannou V, Viggiani G. Strength and dilatancy of natural and reconstituted Vallericca clay. Proc Int Symp on Hard Soils–Soft Rocks, Athens1993. p. 761-768.
[44] Kavvadas M, Amorosi A. A constitutive model for structured soils. Géotechnique. 2000;50:263-273.
[45] Yao Y-P, Kong L-M, Zhou A-N, Yin J-H. Time-dependent unified hardening model: three-dimensional elastoviscoplastic constitutive model for clays. J Eng Mech. 2014;141:04014162.
[46] Liu Y-H, Huang M-S, Li S. An anisotropic bounding surface model for structured soft clay under cyclic loading. Chinese Journal of Geotechnical Engineering. 2010;32:1065-1071.
[47] Qian J-G, Du Z-B, Yin Z-Y. Cyclic degradation and non-coaxiality of soft clay subjected to pure rotation of principal stress directions. Acta Geotech. 2018;13:943-959.
[48] Yin Z-Y, Xu Q, Chang CS. Modeling cyclic behavior of clay by micromechanical approach. J Eng Mech. 2012;139:1305-1309.
[49] Itasca F. Fast Lagrangian analysis of continua. Itasca Consulting Group Inc, Minneapolis, Minn. 2000.
[50] Marti J. Mixed discretization procedure for accurate solution of plasticity problems. Int Jour, Num Methods & Analy Methods in Geomech. 1982:23-26.
[51] Zhang DM, Ma LX, Zhang J, Hicher PY, Juang CH. Ground and tunnel responses induced by partial leakage in saturated clay with anisotropic permeability. Engineering Geology. 2015;189:104-115.
[52] Gang W. Selection and distribution of ground loss ratio induced by shield tunnel construction. Chinese Journal of Geotechnical Engineering. 2010;32:1354-1361.
[53] Lee KM, Ge XW. The equivalence of a jointed shield-driven tunnel lining to a continuous ring structure. Can Geotech J. 2001;38:461-483.
[54] Hefny AM, Chua HC. An investigation into the behaviour of jointed tunnel lining. Tunnelling Underground Space Technol. 2006;21:428.
[55] Teachavorasinskun S, Chub-uppakarn T. Influence of segmental joints on tunnel lining. Tunnelling Underground Space Technol. 2010;25:490-494.
[56] Li L, Zhang B-Q, Yang X-L. Analysis of dynamic response of large cross-section tunnel under vibrating load induced by high speed train. Yanshilixue Yu Gongcheng Xuebao/Chinese Journal of Rock Mechanics and Engineering. 2005;24:4259-4265.

Figure captions

Figure 1 Schematic illustration of the loading and bounding surfaces of the model in triaxial stress space

Figure 2 Mapping rule in bounding surface model

Figure 3 Simulation of oedometer test on Shanghai clay

Figure 4 Simulation of undrained triaxial compression tests on isotropically consolidated Shanghai clay

Figure 5 Simulation of undrained triaxial compression tests on K0-consolidated Shanghai clay

Figure 6 Simulation of oedometer test on Vallericca stiff clay

Figure 7 Simulation of undrained triaxial tests on Vallericca stiff clay

Figure 8 Cyclic undrained triaxial test simulation

733

734